Article

Near-frictionless ion transport within triazine framework membranes

https://doi.org/10.1038/s41586-023-05888-x

Received: 2 August 2022

Accepted: 24 February 2023

Published online: 26 April 2023

Check for updates

Peipei Zuo[1,6], Chunchun Ye[2,6], Zhongren Jiao[1,6], Jian Luo[3], Junkai Fang[1], Ulrich S. Schubert[4,5], Neil B. McKeown[2], T. Leo Liu[3]✉, Zhengjin Yang[1]✉ & Tongwen Xu[1]✉

The enhancement of separation processes and electrochemical technologies such as water electrolysers[1,2], fuel cells[3,4], redox flow batteries[5,6] and ion-capture electrodialysis[7] depends on the development of low-resistance and high-selectivity ion-transport membranes. The transport of ions through these membranes depends on the overall energy barriers imposed by the collective interplay of pore architecture and pore–analyte interaction[8,9]. However, it remains challenging to design efficient, scaleable and low-cost selective ion-transport membranes that provide ion channels for low-energy-barrier transport. Here we pursue a strategy that allows the diffusion limit of ions in water to be approached for large-area, free-standing, synthetic membranes using covalently bonded polymer frameworks with rigidity-confined ion channels. The near-frictionless ion flow is synergistically fulfilled by robust micropore confinement and multi-interaction between ion and membrane, which afford, for instance, a Na^+ diffusion coefficient of 1.18×10^{-9} m^2 s^{-1}, close to the value in pure water at infinite dilution, and an area-specific membrane resistance as low as 0.17 Ω cm^2. We demonstrate highly efficient membranes in rapidly charging aqueous organic redox flow batteries that deliver both high energy efficiency and high-capacity utilization at extremely high current densities (up to 500 mA cm^{-2}), and also that avoid crossover-induced capacity decay. This membrane design concept may be broadly applicable to membranes for a wide range of electrochemical devices and for precise molecular separation.

Selective ion-transport membranes are key components of clean-energy technologies, including large-scale, energy-efficient separation and purification processes and, of course, electrochemical devices as diverse as CO_2 electrolysers and water electrolysers[1,2,10], H_2/O_2 fuel cells[3,4], redox flow batteries[5,6], ion-capture electrodialysis[7] and so on. In all of these well-established and emerging electrochemical systems, membrane separators transport ions and isolate electrochemical reactions in two half-cells, their efficacy being contingent on the ability of membrane separators to perform rapid and selective ion transport[5,11,12]. Ion transport through membranes at subnanometre scales depends on the overall energy barriers, which are determined by nanoconfinement within free-volume voids and pore–ion interactions[8,9]. Therefore, construction of ion channels with low energy barriers is imperative for the development of high-performing membranes in electrochemical processes.

Polymer materials dominate the use of selective ion-transport membranes in practical modules across all scales, due to their ideal combination of low cost, manufacturing scaleability and small footprint. Conventional polymer materials, represented by perfluorocarbon Nafion and the recently developed hydrocarbon-based polyelectrolytes, form ion-conductive regions via microphase separation[13,14]. However, these regions are ill defined and prone to swelling to several nanometres in size following hydration, which may facilitate ion diffusion but also causes poor selectivity (Fig. 1a and Supplementary Fig. 1). The emerging perspective is to confine the size of pore volume voids—that is, to increase the rigidity of the polymer backbone and reduce the thermal motion of the polymer segment—to enforce good size selectivity for rapid ion transport[15]. In particular, solution-processable, semirigid polymers of intrinsic microporosity (PIMs; Fig. 1b) are emerging as next-generation molecule-separation[16,17] and ion-transport membranes[18–23], benefiting from size-exclusion-induced selectivity and free-volume-induced permeability. However, these semirigid, non-network PIMs may age and, at high content of charged functionalities, can undergo severe swelling leading to decreased selectivity[21,24,25].

We therefore aimed to deploy shape-persistent polymer frameworks to apply rigid confinement to free-volume voids, but realized that a well-confined framework alone would be unlikely to provide a mechanism for rapid ion transport. Another key design criterion to reduce energy barriers of ion transport across membranes is to leverage interactions between pore walls and ions to promote frictionless ion transport. Thus, we sought to improve multiple interactions between pores and ions by engineering charged, polar and Lewis acidic/basic moieties into polymer frameworks. Here we report a new family of all-rigid polymer framework membranes containing well-confined ion channels (Fig. 1c,d). Our structural design combines (1) the isolation of absorbed water within microcavities from the hydrophobic backbone framework to facilitate selective ion transport at robust subnanometre confinement and

[1]Key Laboratory of Precision and Intelligent Chemistry, Department of Applied Chemistry, School of Chemistry and Material Science, University of Science and Technology of China, Hefei, P. R. China. [2]EastCHEM School of Chemistry, University of Edinburgh, Edinburgh, UK. [3]Utah State University, Chemistry and Biochemistry, Logan, UT, USA. [4]Laboratory of Organic and Macromolecular Chemistry, Friedrich Schiller University Jena, Jena, Germany. [5]Center for Energy and Environmental Chemistry Jena, Friedrich Schiller University Jena, Jena, Germany. [6]These authors contributed equally: Peipei Zuo, Chunchun Ye, Zhongren Jiao. ✉e-mail: leo.liu@usu.edu; yangzj09@ustc.edu.cn; twxu@ustc.edu.cn

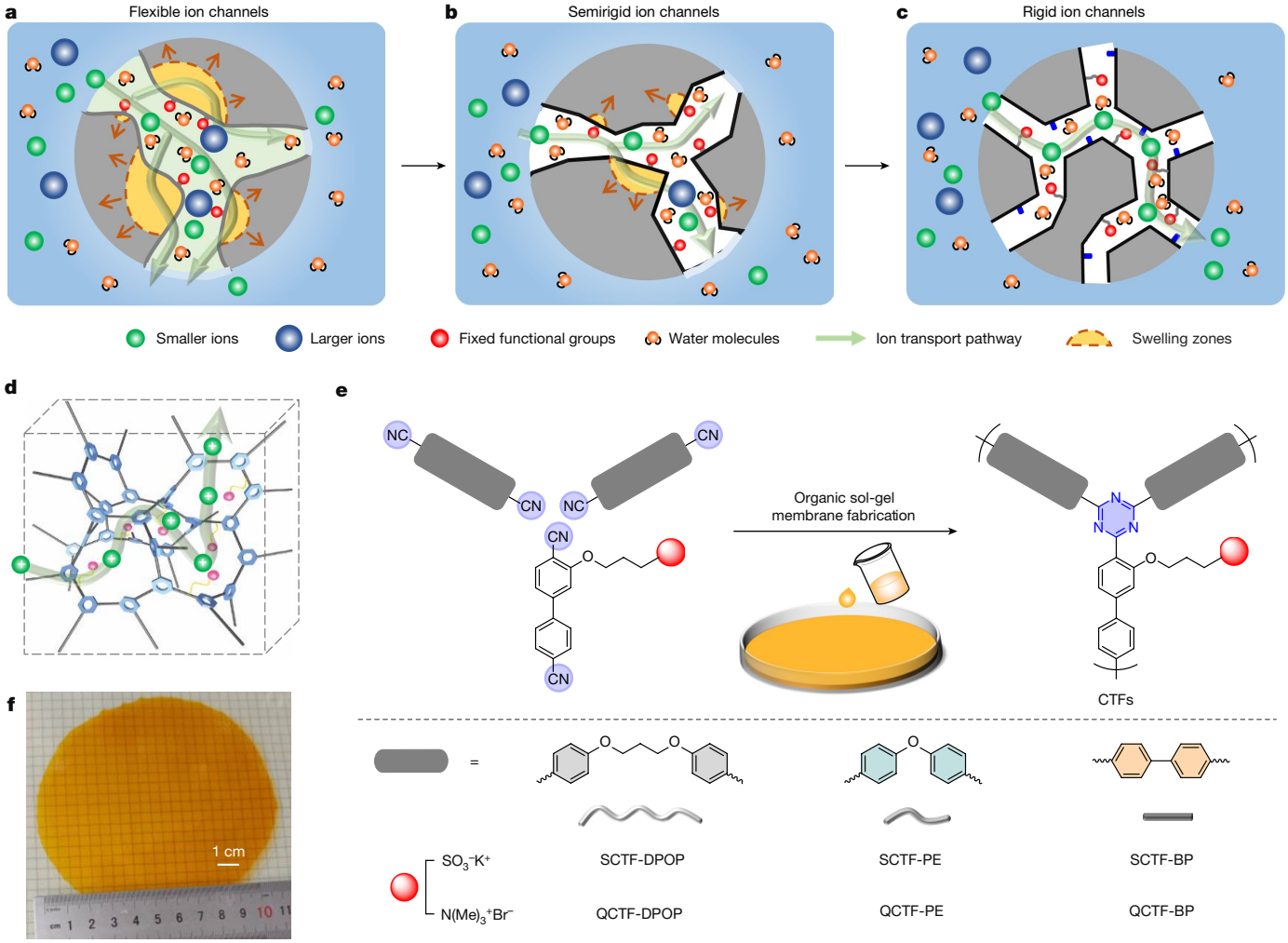

Fig. 1 | Schematic illustrations showing existing and proposed ion-selective polymer membranes with varying ion channels. a, Membranes with flexible ion channels. These contain microphase-separated morphology derived from the assembly of hydrophilic ion-conductive moieties and hydrophobic flexible-polymer backbones, represented by Nafion. **b**, Ion-selective microporous membranes with semirigid ion channels. The channels are formed by intrinsic micropores resulting from inefficient polymer chain packing, represented by polymers of intrinsic microporosity and their derivatives. To render the membrane ion conductive, functional moieties are incorporated during postsynthetic modification. Membranes may age over time and swell in water. **c**,**d**, Our proposed membranes with rigid ion channels (**c**). These are expected to build from bottom-up synthesis and via swelling-resistant 3D polymer frameworks (**d**). Pore architecture and chemistry are tuned for rapid and selective ion transport. **e**,**f**, Preparation of stand-alone CTF membranes via a superacid-catalysed organic sol-gel reaction from functional aromatic nitrile monomers (**e**). CTF membranes have a controlled number of ion-conductive moieties inside membrane pores and a covalent network structure. Image (**f**) shows a free-standing CTF membrane with a diameter of over 10 cm. Structure rigidity and microporosity of the CTF membrane can be regulated by designing variable structural units, as demonstrated at bottom right, from flexible to very rigid.

(2) multiple interactions between ions and pore walls to synergistically approach the diffusion limit of ions based on coordination mechanisms. We exemplify this concept via the fabrication of covalent triazine framework (CTF) membranes whose channel size, as well as channel chemistry, can be finely-tuned. We find that these polymer framework membranes exhibit ultrahigh ion diffusivity but also extremely low permeability of active materials. Using flow battery technology for exemplification, CTF membranes fulfilled their functions as efficient ion-transport membrane separators providing flow batteries with ultrafast charging capacity.

The CTF membranes are constructed from functional aromatic nitrile monomers via a superacid-catalysed organic sol-gel reaction[26,27] (Fig. 1e,f and Supplementary Figs. 2–4). Self-standing CTF membranes are readily formed on a large scale during the polymerization reaction with concomitant microporosity at the narrow subnanometre scale (Supplementary Fig. 5). Pore geometry is readily regulated by the appropriate choice of monomer structural units with varying rigidity; pore chemistry is adjusted by adopting different types of functional groups (that is, negatively, positively and neutrally charged moieties) and by controlling the amount of ion-conductive moieties (that is, ion-exchange capacity, IEC) to afford corresponding cation-conductive membranes (SCTFs) and anion-conductive membranes (Fig. 1e and Supplementary Fig. 3). Importantly short, flexible spacers are applied to connect nitrile monomers to charged functional groups, thereby mitigating their electron-withdrawing effects and enabling the trimerization reaction of aromatic nitriles. Details of CTF synthesis and spectroscopic characterization are provided in the Supplementary Information. The mechanical properties of the resulting polymer membranes were measured by tensile testing (Supplementary Fig. 5), showing Young's modulus and the ultimate tensile strength of SCTF-biphenyl (SCTF-BP) membranes as high as 1.1 GPa and 29 MPa, respectively.

Moderate CO_2 uptake of the SCTF-BP sample at low pressure and 273 K confirmed the accessible microporosity of the three-dimensional (3D) framework structure (Fig. 1d and Supplementary Fig. 6). Notably, SCTF-BP has lower CO_2 adsorption than classical semirigid PIM-1 (the

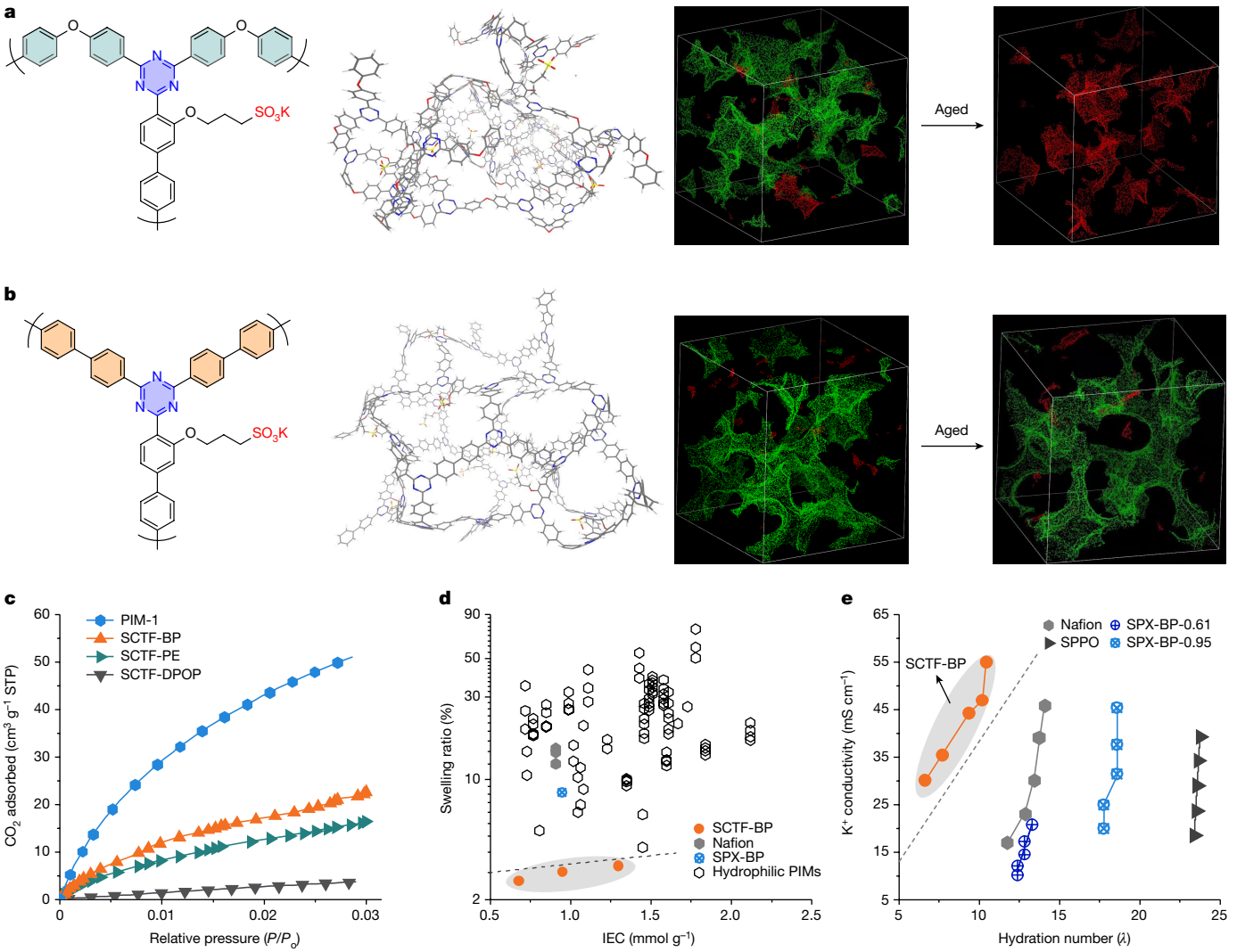

Fig. 2 | Characterization of negatively charged CTF membranes (SCTF). **a**,**b**, Schematic representation of the chain structure of SCTF-PE (**a**) and SCTF-BP (**b**), with a flexible and a very rigid chain, respectively (left). 3D view of the amorphous cells of SCTF-PE and SCTF-BP membranes (middle). Images of aged cells shown on the right. Red shading represents isolated free-volume elements and green shading represents interconnected micropores. **c**, CO_2 uptake (at 273 K) of SCTF samples compared with that of PIM-1. **d**, Swelling ratio plotted as a function of IEC (the content of charged functional groups, in mmol g^{-1}) for SCTF-BP, Nafion, SPX-BP and hydrophilic PIM membranes. **e**, K^+ conductivity plotted as a function of hydration number for SCTF-BP, Nafion, SPX-BP and SPPO membranes. Each dot represents measurement at a separate temperature: from left to right, 30–70 °C. Dashed lines and shading are a visual guide only. **d**,**e**, The values shown can be found in Supplementary Tables 1 and 3. STP, standard temperature and pressure.

archetypal PIM polymer), suggesting the smaller size of free-volume elements in SCTF-BP, and predominately subnanometre-sized pore size distribution was confirmed using positron annihilation lifetime spectroscopy (Supplementary Fig. 6), which would improve the size selectivity of ion transport. Micropore size distribution of the resulting membranes is regulated by adopting monomers of varying rigidity (Fig. 2a–c and Supplementary Fig. 7). SCTF-BP constructed from rigid monomers can provide almost one order of magnitude higher cumulative pore volume in comparison with that of SCTF-diphenoxypropane (SCTF-DPOP) fabricated using flexible monomers, as visualized from molecular simulations of the accessible free-volume elements of SCTF-BP compared with other CTF membranes (Fig. 2a,b and Supplementary Figs. 8 and 9). After ageing these cell models with a forcefield, highly rigid SCTF-BP retained the most interconnected volume elements, suggesting its enhanced anti-swelling capacity (Fig. 2a,b and Supplementary Fig. 9). X-ray diffraction analysis showed that SCTF-BP has similar scattering peaks in dry and swelling states, indicating that interchain distance does not change following water uptake (Supplementary Fig. 6c, right). A control experiment performed on SPX-BP, a PIM with the same biphenyl linkage as SCTF-BP, showed the disappearance of distinct scattering peaks owing to the obvious swelling of the membrane (Supplementary Figs. 6c (left) and 10). Indeed, the SCTF-BP membrane has an extremely low swelling ratio in comparison with both commercial ion-exchange membranes and reported PIM membranes, in which high IEC values are correlated with severe swelling, thus compromising membrane selectivity (Fig. 2d and Supplementary Table 1).

The robust framework structure with subnanometre micropores can effectively block the permeation of redox-active electrolytes through the SCTF-BP membrane. Over the temperature range of 25–60 °C, the permeability of 2,6-dihydroxyanthraquinone (DHAQ) is at least one order of magnitude lower, and that of $K_4[Fe(CN)_6]$ is two orders of magnitude lower through SCTF-BP, than Nafion 212 (Supplementary Figs. 11 and 12 and Supplementary Table 2; see Supplementary Information for pretreatment of Nafion membrane samples; note that Nafion properties may vary significantly with pretreatment). Such low permeabilities of

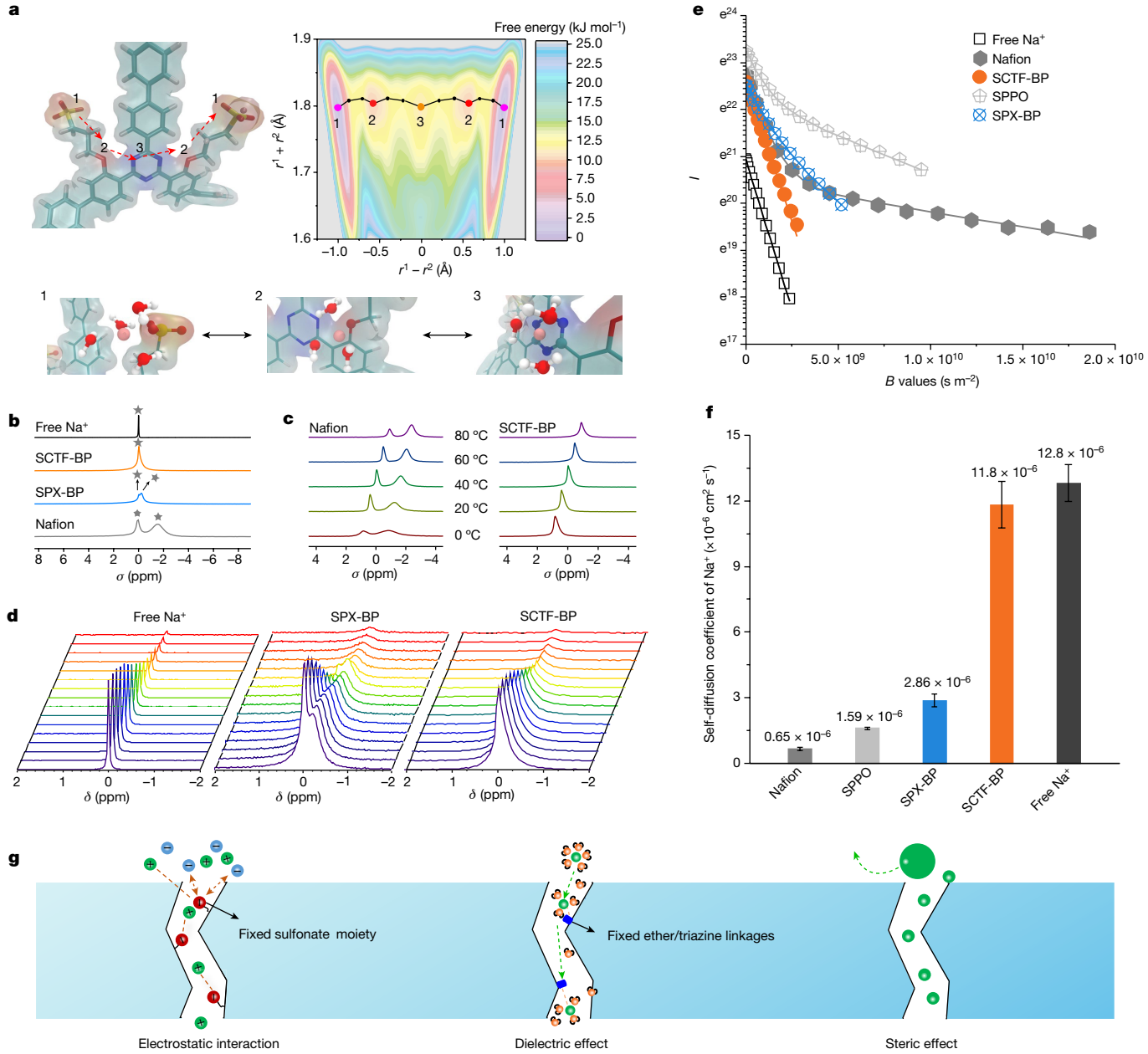

Fig. 3 | Ion transport across the SCTF-BP membrane. a, Modelling and calculation of free energy for the transport of K^+ across the SCTF-BP membrane matrix; the path 1-2-3-2-1 has the lowest free energy for K^+ transport. Insets demonstrate the specific interaction between K^+ and SCTF-BP chains in positions 1, 2 and 3. **b**, ssNMR measured for membrane samples of SCTF-BP, SPX-BP and Nafion. 100 mM NaCl in water was used as control, with membrane samples immersed in 0.1 M NaCl solution (Na^+ rather than K^+ because of improved NMR sensitivity). **c**, ^{23}Na ssNMR for Nafion and SCTF-BP membranes in 0.1 M NaCl solution at varying temperature. **d**, PFG–NMR spectra collected for 0.1 M NaCl solution and membrane samples of SPX-BP and SCTF-BP. Spectra for Nafion and SPPO are given in Supplementary Fig. 20. **e**,**f**, Plot of PFG–NMR signal intensity versus magnetic gradient strength (**e**, *B* values) and diffusion coefficients derived from PFG–NMR for Na^+ in water, SCTF-BP, SPX-BP, Nafion and SPPO membrane samples (**f**). Echo profiles are fitted to the Stejskal–Tanner equation. *I* denotes the echo height at a given gradient strength; *B* denotes the product of all parameters before the diffusion coefficient (*D*) of the Stejskal–Tanner equation (that is, equation 9 in Supplementary Information); r^1 and r^2 denote the distance between the potassium ion and the geometric centre of two adjacent sulfonate groups. Error bars (s.d.) are derived from three measurements based on three individual membrane samples. **g**, Schematic showing electrostatic interaction and dielectric and steric effects during ion transport enabled by the negatively charged CTF membrane.

active species, even at the high temperature of 60 °C, are envisioned as affording the SCTF-BP flow cell a decadal operational lifetime (Supplementary Fig. 12). Importantly, SCTF-BP membranes demonstrate rapid transport of charge carriers, with the most conductive K^+ showing a cation transference number (t_+) as high as 0.988 (Supplementary Fig. 13). The K^+ conductivity of the SCTF-BP membrane, as measured by four-point electrochemical impedance spectroscopy (EIS), approached 30 mS cm^{-1} at 30.0 °C and 54.9 mS cm^{-1} at 70 °C at low hydration number (6.7 at 30 °C, 10.5 at 70 °C; Fig. 2e, Supplementary Fig. 14 and Supplementary Table 3). Notably, for existing membranes with extremely low electrolyte permeability (for example, Fumasep E-620(K)), K^+ conductivity is far lower than that of SCTF-BP (Supplementary Fig. 15).

To explain this exceptionally high ionic conductivity, the K^+ transport pathway along the polymeric backbone of SCTF-BP was optimized and the two-dimensional free-energy landscape was generated based on the reported computational methodology (Fig. 3a and Supplementary

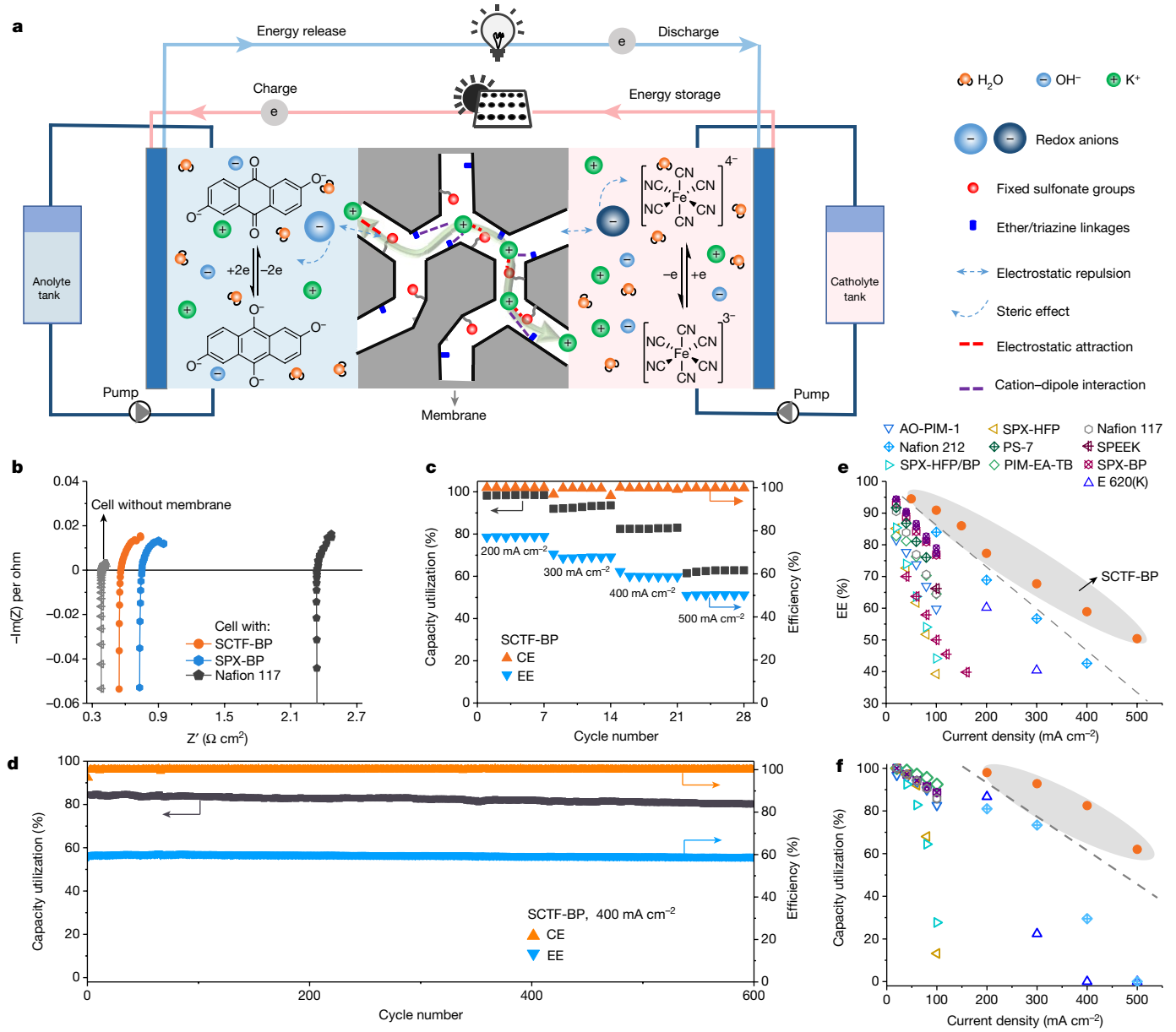

Fig. 4 | SCTF-BP membrane enables rapid charging of aqueous alkaline quinone flow battery. a, Schematic illustrating an alkaline quinone flow battery assembled with the SCTF-BP membrane, and conduction of K^+ ions across the membrane matrix. The catholyte is ferrocyanide and the anolyte molecule is DHAQ. **b**, EIS spectra measured in cells assembled with SCTF-BP, SPX-BP and Nafion 117 membrane, respectively. The grey line represents the EIS spectrum of the cell without a membrane. **c**, Coulombic efficiency (CE), capacity utilization and EE of the cell assembled with SCTF-BP at varying current density. For each current density, seven repetitions were performed to ensure accuracy. Fluctuations were observed only when current density was switched. **d**, Galvanostatic cycling at a current density of 400 mA cm^{-2} for cells assembled with a SCTF-BP membrane. **b**–**d**, Electrolyte concentration 0.4 M. **e**,**f**, Energy efficiency (**e**) and capacity utilization (**f**) of quinone flow batteries assembled with commercial, PIM and SCTF-BP membranes are plotted as functions of current density. Symbols shown in inset in **e** apply also to **f**. **e**,**f**, Dashed lines and shading are a visual guide only; detailed values provided in Supplementary Table 5.

Fig. 16)[23]. This shows the lowest energy barrier, with the critical steps involving the electrostatic interaction and dielectric interaction of K^+ ions with sulfonate groups and ether/triazine linkages, respectively. This is in good agreement with the simulation of mean square displacement for K^+ diffusion in SCTF membranes (Supplementary Fig. 17).

The computational work is supported by systematic NMR studies (^{23}Na NMR was applied due to its higher sensitivity compared with K). ^{23}Na NMR can show the ion–dipole interaction between Na^+ ions and model triazine molecules in an aqueous solution (Supplementary Fig. 18). ^{23}Na magic-angle-spinning solid-state NMR (^{23}Na ssNMR) shows two separate Na^+ signals for Nafion and SPX-BP membranes (Fig. 3b), with the downfield signal suggesting free Na^+ (located at the same position as that in 100 mM aqueous NaCl solution) and the upfield signal corresponding to Na^+ within membrane pores[19]. By contrast, only the downfield signal suggested that free Na^+ is detected for the SCTF-BP membrane (Fig. 3b). Notably, the full width at half maximum of the peak remains narrow and almost unchanged for SCTF-BP at 0–80 °C in the temperature-varied ^{23}Na ssNMR experiments, whereas an obvious 'motional' narrowing of the peak was observed for Nafion with increasing temperature (Fig. 3c and Supplementary Fig. 19). This line shape represents the temporally averaged local environment, which is closely related to the mobility of Na^+.

The mobility (diffusion coefficient) of Na^+ through these membranes was further measured by pulsed-field gradient–stimulated-echo nuclear magnetic resonance (PFG–NMR) experiments (Fig. 3d and Supplementary Fig. 20). By fitting echo profiles with the Stejskal–Tanner equation[28] (Fig. 3e) the calculated Na^+ diffusion coefficient of SCTF-BP is 1.18×10^{-9} m^2 s^{-1}, which is at least one order of magnitude greater than that of Nafion, SPPO and SPX-BP (6.50×10^{-11}, 1.59×10^{-10} and 2.86×10^{-10} m^2 s^{-1}, respectively; Fig. 3f). Indeed, such high Na^+ mobility is close to the measured diffusion coefficient of Na^+ in water (1.28×10^{-9} m^2 s^{-1}; Fig. 3f), even at infinite dilution (1.33×10^{-9} m^2 s^{-1}), which can be considered as free diffusion and attests to the secondary interactions between cations and the pore wall surface and steric effect (Fig. 3g).

The advantages of CTF materials serving as selective ion-transport membranes were exemplified using aqueous organic redox flow batteries (AORFBs). For this application a membrane separator acts as both electrolyte insulator and charge carrier conductor between two half-cells (Fig. 4a). Current AORFBs can operate only at relatively low current densities, mostly at 100 mA cm^{-2} or less, due to the high membrane resistance caused by the impeded diffusion of charge carrier ions traversing synthetic ion-exchange membranes. To assess the performance of SCTF-BP as a membrane separator in the alkaline quinone AORFB, full-flowing cells were assembled based on 2,6-DHAQ/$K_4Fe(CN)_6$ electrolytes and tested at both low (0.1 M) and high (0.4 M) electrolyte concentration (Fig. 4 and Supplementary Figs. 21 and 22). As controls, otherwise identical cells with commercial Nafion 117, Nafion 212 and Fumasep E-620(K) were assembled (Supplementary Figs. 23–26). The cell running at 0.1 M electrolyte concentration based on the SCTF-BP membrane showed a capacity utilization of over 85% at a current density of 120 mA cm^{-2} (Supplementary Fig. 21); however, the cell using Nafion 117 could not even operate/cycle at the same current density, which shows capacity utilization decreasing sharply from 94.2 to 34.5% with current density increasing from 40 to 100 mA cm^{-2} (Supplementary Fig. 23). The enhanced performance found with the SCTF-BP membrane is ascribed to its remarkably low resistance of 0.53 Ω cm^2, as shown by high-frequency EIS in cells operating at 50% state of charge (Supplementary Figs. 21 and 22). By further subtracting contributions from other components, the neat SCTF-BP membrane shows an areal-specific resistance as low as 0.17 Ω cm^2 (Fig. 4b) at an electrolyte concentration of 0.4 M and contributes only 20.7% of polarization resistance for the whole cell, which is much lower than that of Nafion 117, Nafion 212 and Fumasep E-620(K) in otherwise identical cells (Supplementary Table 4 and Supplementary Figs. 24–26).

Such a low resistance of the SCTF-BP membrane enables cell operation at extreme current densities, from 200 to 500 mA cm^{-2}, but also shows exceptionally high energy efficiency (round-trip) and high-capacity utilization at 0.4 M electrolyte concentration (Fig. 4c–f). For example, this cell achieved capacity utilization of 62% and an energy efficiency (EE) of 50.4% at current density up to 500 mA cm^{-2} (Fig. 4c), approaching the levels of acidic quinone AORFBs in which the charge carrier (H^+) diffuses much more rapidly than K^+ (ref. 29), confirming the potential of SCTF-BP membranes for rapid charging of alkaline quinone AORFBs. Furthermore, flow batteries based on the SCTF-BP membrane achieved long-term galvanostatic cell operation over 5,000 cycles at 160 mA cm^{-2} using 0.1 M electrolyte concentration (Supplementary Fig. 21), and over 600 cycles at 400 mA cm^{-2} using 0.4 M electrolyte concentration (Fig. 4d). In addition to low membrane resistance, the SCTF-BP membrane can effectively block the cross-contamination of active species during cell cycling at both room temperature and 45 °C (Supplementary Fig. 27 and Supplementary Table 6). The exceptional performance of alkaline AORFBs encouraged us to extend the application of CTF membranes to pH-neutral AORFBs using nitroxide radical/viologen-based redox chemistry (Supplementary Figs. 28 and 29). It is clear that our CTF membranes enable both alkaline and pH-neutral AORFBs to perform rapid charging at extreme current density with concomitantly high EE and high-capacity utilization. These data far exceed those for otherwise identical cells assembled with commercial membranes and state-of-the-art ion-sieving membranes (Supplementary Tables 5, 7 and 8).

To conclude, microporous CTF membranes—derived from aromatic nitrile monomers with different charge functionalities through a superacid-catalysed organic sol-gel process—achieved high-performing AORFBs for a range of redox chemistries, attributable to the low energy barriers for cation diffusion through well-confined micropores. This design strategy may be broadly applicable considering the various options of organic reactions and monomers in construction of covalent organic frameworks. We anticipate that these CTF membranes will enable a broader range of applications beyond those presently demonstrated in AORFBs—for instance, in electrochemical devices for CO_2 reduction[10]. Although a local frictionless ion flow related to the wettability of 3D nanochannels[30] was observed within the SCTF-BP membrane, further manipulations of CTF membrane architectures are required to facilitate long-range ion diffusion, which may be hindered by pore tortuosity. The concept we propose here extends the potential of ultrafast ion-conducting membranes beyond inorganic microporous counterparts (for example, zeolites, carbon nanotubes, graphene and MXenes) and suggests opportunities for the development of polymer membranes relying on secondary interactions for precise molecular separation.

Online content

Any methods, additional references, Nature Portfolio reporting summaries, source data, extended data, supplementary information, acknowledgements, peer review information; details of author contributions and competing interests; and statements of data and code availability are available at https://doi.org/10.1038/s41586-023-05888-x.

1. Salvatore, D. A. et al. Designing anion exchange membranes for CO_2 electrolysers. *Nat. Energy* **6**, 339–348 (2021).
2. Lagadec, M. F. & Grimaud, A. Water electrolysers with closed and open electrochemical systems. *Nat. Mater.* **19**, 1140–1150 (2020).
3. Jiao, K. et al. Designing the next generation of proton-exchange membrane fuel cells. *Nature* **595**, 361–369 (2021).
4. Tang, H. et al. Fuel cells with an operational range of –20 °C to 200 °C enabled by phosphoric acid-doped intrinsically ultramicroporous membranes. *Nat. Energy* **7**, 153–162 (2022).
5. Xiong, P., Zhang, L., Chen, Y., Peng, S. & Yu, G. A chemistry and microstructure perspective on ion-conducting membranes for redox flow batteries. *Angew. Chem. Int. Ed. Engl.* **60**, 24770–24798 (2021).
6. Zhang, L., Feng, R., Wang, W. & Yu, G. Emerging chemistries and molecular designs for flow batteries. *Nat. Rev. Chem.* **6**, 524–543 (2022).
7. Uliana, A. A. et al. Ion-capture electrodialysis using multifunctional adsorptive membranes. *Science* **372**, 296–299 (2021).
8. Epsztein, R., DuChanois, R. M., Ritt, C. L., Noy, A. & Elimelech, M. Towards single-species selectivity of membranes with subnanometre pores. *Nat. Nanotechnol.* **15**, 426–436 (2020).
9. Zhou, X. et al. Intrapore energy barriers govern ion transport and selectivity of desalination membranes. *Sci. Adv.* **6**, eabd9045 (2020).
10. Lees, E. W., Mowbray, B. A. W., Parlane, F. G. L. & Berlinguette, C. P. Gas diffusion electrodes and membranes for CO_2 reduction electrolysers. *Nat. Rev. Mater.* **7**, 55–64 (2021).
11. Ran, J. et al. Ion exchange membranes: new developments and applications. *J. Membr. Sci.* **522**, 267–291 (2017).
12. Foglia, F. et al. Disentangling water, ion and polymer dynamics in an anion exchange membrane. *Nat. Mater.* **21**, 555–563 (2022).
13. Shin, D. W., Guiver, M. D. & Lee, Y. M. Hydrocarbon-based polymer electrolyte membranes: importance of morphology on ion transport and membrane stability. *Chem. Rev.* **117**, 4759–4805 (2017).
14. Kusoglu, A. & Weber, A. Z. New insights into perfluorinated sulfonic-acid ionomers. *Chem. Rev.* **117**, 987–1104 (2017).
15. Park, H. B., Kamcev, J., Robeson, L. M., Elimelech, M. & Freeman, B. D. Maximizing the right stuff: the trade-off between membrane permeability and selectivity. *Science* **356**, eaab0530 (2017).
16. Thompson, K. A. et al. N-Aryl–linked spirocyclic polymers for membrane separations of complex hydrocarbon mixtures. *Science* **369**, 310–315 (2020).
17. Lai, H. W. H. et al. Hydrocarbon ladder polymers with ultrahigh permselectivity for membrane gas separations. *Science* **375**, 1390–1392 (2022).
18. Baran, M. J. et al. Design rules for membranes from polymers of intrinsic microporosity for crossover-free aqueous electrochemical devices. *Joule* **3**, 2968–2985 (2019).

19. Tan, R. et al. Hydrophilic microporous membranes for selective ion separation and flow-battery energy storage. *Nat. Mater.* **19**, 195–202 (2020).
20. Zuo, P. et al. Sulfonated microporous polymer membranes with fast and selective ion transport for electrochemical energy conversion and storage. *Angew. Chem. Int. Ed. Engl.* **59**, 9564–9573 (2020).
21. Ye, C. et al. Development of efficient aqueous organic redox flow batteries using ion-sieving sulfonated polymer membranes. *Nat. Commun.* **13**, 3184 (2022).
22. Ye, C. et al. Long-life aqueous organic redox flow batteries enabled by amidoxime-functionalized ion-selective polymer membranes. *Angew. Chem. Int. Ed. Engl.* **61**, e202207580 (2022).
23. Baran, M. J. et al. Diversity-oriented synthesis of polymer membranes with ion solvation cages. *Nature* **592**, 225–231 (2021).
24. Low, Z. X., Budd, P. M., McKeown, N. B. & Patterson, D. A. Gas permeation properties, physical aging, and its mitigation in high free volume glassy polymers. *Chem. Rev.* **118**, 5871–5911 (2018).
25. Koros, W. J. & Zhang, C. Materials for next-generation molecularly selective synthetic membranes. *Nat. Mater.* **16**, 289–297 (2017).
26. Zhu, X. et al. A superacid-catalyzed synthesis of porous membranes based on triazine frameworks for CO_2 separation. *J. Am. Chem. Soc.* **134**, 10478–10484 (2012).
27. Yang, Z. et al. Surpassing Robeson upper limit for CO_2/N_2 separation with fluorinated carbon molecular sieve membranes. *Chem* **6**, 631–645 (2020).
28. Johnson, C. S. Jr Diffusion ordered nuclear magnetic resonance spectroscopy: principles and applications. *Prog. Nucl. Magn. Reson. Spectrosc.* **34**, 203–256 (1999).
29. Huskinson, B. et al. A metal-free organic-inorganic aqueous flow battery. *Nature* **505**, 195–198 (2014).
30. Zhang, X., Liu, H. & Jiang, L. Wettability and applications of nanochannels. *Adv. Mater.* **31**, 1804508 (2019).

Data availability

The data that support the findings of this study are available in the manuscript and its Supplementary Information, and also from the corresponding authors on reasonable request.

Acknowledgements This work was financially supported by the National Key Research and Development Project (nos. 2021YFB4000300 and 2020YFB1505600) and the National Natural Science Foundation of China (nos. 21922510, 21878281, U20A20127 and 52021002). T.L.L. and J.L. acknowledge financial support by the National Science Foundation (career award, grant no. 1847674). N.B.M. and C.Y. thank the Engineering and Physical Science Research Council for funding through programme grant SynHiSel (no. EP/V047078). P.Z. acknowledges financial support by the China Postdoctoral Science Foundation (no. 2021M693066) and Fundamental Research Funds for the Central Universities (no. WK2060000028). The authors thank H. Zhang for help with positron annihilation lifetime spectroscopy experiments. Z.Y. thanks the support of his wife, Q. Fang, and his sons, G.-C. Yang and G.-Q. Yang, during the difficult time of the COVID-19 pandemic.

Author contributions Z.Y. and T.X. conceived and directed the project. T.L.L. provided suggestions and guidance during project implementation. P.Z., C.Y. and J.F. conducted experiments. Z.J. performed molecular simulations. P.Z., C.Y., Z.J., J.L., T.L.L., Z.Y. and T.X. analysed and discussed data. P.Z., C.Y., Z.J., Z.Y. and T.X. wrote the manuscript with input from T.L.L., J.L., J.F., U.S.S. and N.B.M. All authors offered constructive feedback on the manuscript.

Competing interests The authors declare no competing interests.

Additional information

Supplementary information The online version contains supplementary material available at https://doi.org/10.1038/s41586-023-05888-x.

Correspondence and requests for materials should be addressed to T. Leo Liu, Zhengjin Yang or Tongwen Xu.

Peer review information *Nature* thanks Young Moo Lee and the other, anonymous, reviewer(s) for their contribution to the peer review of this work.